

1 Article

2 

# Dynamic Virtual Simulation with Real-time Haptic Feedback 3 for Robotic Internal Mammary Artery Harvesting

4 Shuo Wang <sup>1,†</sup>, Tong Ren<sup>2,3,†</sup>, Nan Cheng<sup>2</sup>, Rong Wang <sup>2,\*</sup>, and Li Zhang <sup>1,\*</sup>

5

6

7

8

9

10

11

12

13

14

15

16

<sup>1</sup> Department of Engineering Physics, Key Laboratory of Particle and Radiation Imaging, Ministry of Education, Tsinghua University, Beijing, China; zli@mail.tsinghua.edu.cn(L.Z.); [shuo-wan19@mails.tsinghua.edu.cn](mailto:shuo-wan19@mails.tsinghua.edu.cn)(S.W.)

<sup>2</sup> Department of Adult Cardiac Surgery, Senior Department of Cardiology, The Six Medical Center of PLA General Hospital, Fucheng Road, Haidian District, 100048, Beijing, China; wangrongd@126.com(R.W.); cn86919@163.com(N.C.); rentong8713@163.com(T.R.)

<sup>3</sup> Chinese PLA Medical School, Fuxing Road, Haidian District, 100089, Beijing, China; ren-tong8713@163.com(T.R.)

\* Correspondence: wangrongd@126.com(R.W.); [zli@mail.tsinghua.edu.cn](mailto:zli@mail.tsinghua.edu.cn)(L.Z.); Tel.: +86-13910686306(L.Z.)

† These authors contributed equally to this work.

**Abstract:** Coronary heart disease, a leading global cause of mortality, has witnessed significant advancement through robotic coronary artery bypass grafting (CABG), with the internal mammary artery (IMA) emerging as the preferred "golden conduit" for its exceptional long-term patency. Despite these advances, robotic-assisted IMA harvesting remains challenging due to the absence of force feedback, complex surgical maneuvers, and proximity to the beating heart. This study introduces a novel virtual simulation platform for robotic IMA harvesting that integrates dynamic anatomical modeling and real-time haptic feedback. By incorporating a dynamic cardiac model into the surgical scene, our system precisely simulates the impact of cardiac pulsation on thoracic cavity operations. The platform features high-fidelity representations of thoracic anatomy and soft tissue deformation, underpinned by a comprehensive biomechanical framework encompassing fascia, adipose tissue, and vascular structures. Our key innovations include a topology-preserving cutting algorithm, bidirectional tissue coupling mechanism, and dual-channel haptic feedback for electrocautery simulation. Quantitative assessment using our newly proposed Spatial Asymmetry Index (SAI) demonstrated significant behavioral adaptations to cardiac motion, with dynamic scenarios yielding superior SAI values compared to static conditions. These results validate the platform's potential as an anatomically accurate, interactive, and computationally efficient solution for enhancing surgical skill acquisition in complex cardiac procedures.

Academic Editor: Firstname Last- 33  
name

Received: date

Revised: date

Accepted: date

Published: date

Citation: To be added by editorial  
staff during production. 38

Copyright: © 2025 by the authors. 39  
Submitted for possible open access 40  
publication under the terms and 41  
conditions of the Creative Commons 42  
Attribution (CC BY) license 43  
(<https://creativecommons.org/licenses/by/4.0/>). 44

**Keywords:** Robotic cardiac surgery; Coronary artery bypass grafting; Internal mammary artery; Surgical training; Haptic feedback

## 1. Introduction

According to the latest statistics from the World Health Organization (WHO), coronary heart disease has consistently remained the leading cause of death globally over the past decade, accounting for 16.7% of total mortality [1]. With continuous advancements in medical technology, robotic cardiac surgery, representing the pinnacle of minimally invasive surgical techniques, has gained widespread adoption worldwide due to its proven efficacy, minimal invasiveness, and accelerated patient recovery [2]. Robotic

45 CABG constitutes a crucial component of robotic cardiac surgical procedures. In these  
46 operations, the IMA has earned the moniker "golden conduit" due to its exceptional clinical  
47 outcomes. Research data demonstrates that the IMA, when used as a bypass graft,  
48 exhibits superior long-term patency rates, with 10-year patency rates exceeding 90% [3].  
49 This remarkable advantage has established the IMA as the preferred conduit for coronary  
50 bypass procedures. Robotic-assisted IMA harvesting has achieved widespread recogni-  
51 tion and implementation globally, attributed to several key technological advantages:  
52 high-definition 3D imaging systems providing superior surgical visualization, multi-de-  
53 gree-of-freedom robotic instruments offering enhanced dexterity and precise manipula-  
54 tion, and ergonomic control interfaces reducing surgeon fatigue [4]. These features collec-  
55 tively contribute to improved surgical outcomes and operator comfort during these com-  
56 plex procedures.

57 Robotic cardiac surgery, characterized by its master-slave operation mode, presents  
58 unique challenges due to the absence of force feedback and the requirement for complex,  
59 precise surgical maneuvers. Even surgeons with extensive experience in open and thora-  
60 coscopic procedures must overcome a steep initial learning curve. In the context of ro-  
61 botic-assisted minimally invasive CABG, which represents the most frequently performed  
62 robotic cardiac procedure, achieving expertise requires accumulating experience from ap-  
63 proximately 250 cases [5]. Traditionally, cardiac surgery trainees could only acquire tech-  
64 nical skills through direct operating room experience. This apprenticeship model presents  
65 several limitations, including restricted training opportunities and potential risks associ-  
66 ated with adverse events [6]. However, simulation-based training programs have demon-  
67 strated significant efficacy in enhancing technical proficiency, communication skills, and  
68 decision-making capabilities in cardiothoracic surgery [7]. Virtual reality (VR) simulators  
69 offer distinct advantages over animal models and dry-lab simulators. These advantages  
70 include high reproducibility, superior fidelity, unlimited usage potential without physical  
71 deterioration, and the ability to pause, replay, and restart scenarios at will, facilitating  
72 iterative practice and error analysis [8]. Through the development of personalized, inter-  
73 active anatomical models, VR simulation provides core technological support across the  
74 entire spectrum of smart healthcare applications, including surgical skill training, com-  
75 puter-aided diagnosis, and preoperative planning. Consequently, VR simulation is widely  
76 regarded as the most promising solution for robotic surgical skill acquisition [9]. Never-  
77 theless, current virtual reality simulators face several technical challenges, including ac-  
78 curacy in anatomical structure modeling, realism in tissue deformation simulation, au-  
79 thenticity of haptic feedback, and requirements for real-time system performance [10].

80 To enhance surgical simulation fidelity, various physics-based approaches have been  
81 explored for soft-tissue modeling and cutting simulation. The finite element method (FEM)  
82 has demonstrated its capability in achieving precise tissue interactions and flexible defor-  
83 mations [11], with frameworks like SOFA providing robust implementation solutions [12].  
84 Position-based dynamics (PBD), on the other hand, offers an alternative approach that  
85 balances computational efficiency with physical accuracy [13,14]. Notable implemen-  
86 tations include Nvidia FleX and The interactive medical simulation toolkit (iMSTK) [15].  
87 However, traditional organ modeling approaches often treat anatomical structures as iso-  
88 lated entities, overlooking the complex physiological relationships between organs. Such  
89 simplified approaches fail to accurately reflect tissue response characteristics in real sur-  
90 gical environments. Therefore, developing a modeling methodology that effectively inte-  
91 grates physiological constraints and captures dynamic coupling relationships between tis-  
92 sues is crucial for improving the simulation accuracy of virtual surgical systems.

93 Haptic feedback has become a key focus in virtual surgical simulation, enabling sur-  
94 geons to perceive tactile sensations during instrument-tissue interactions [16,17]. While  
95 successfully implemented in systems like the da Vinci Xi, achieving high-quality haptic

96 feedback in virtual simulations faces challenges including real-time computation versus  
97 accuracy trade-offs, complex tissue mechanical modeling, and system latency issues af-  
98 fecting feedback synchronization.

99 Based on these considerations, this study addresses the unique surgical challenges  
100 posed by the internal mammary artery's proximity to the beating heart, where cardiac  
101 pulsation transmitted through the thoracic cavity significantly restricts operating space  
102 and impacts instrument control. We developed a comprehensive virtual simulation envi-  
103 ronment for internal mammary artery harvesting, incorporating both anatomical relation-  
104 ships and cardiac motion effects. The system successfully implements various surgical  
105 interactions including soft tissue deformation, tissue cutting, and removal operations.  
106 This research provides novel insights and practical experience for the further develop-  
107 ment of virtual surgical simulation systems, particularly in accurately replicating the com-  
108 plex dynamics of thoracic surgical procedures.

## 109 2. Materials and Methods

110 We propose the design, development and evaluation of a haptic-enabled virtual sim-  
111 ulation platform for robotic IMA harvesting. The system integrates essential hardware  
112 components including dual haptic interfaces for bimanual instrument control, foot pedals  
113 for electrocautery activation, and high-resolution displays for 3D visualization, as shown  
114 in Figure 1. A dedicated software interface enables precise control of virtual robotic in-  
115 struments with real-time force feedback during tissue manipulation and dissection. The  
116 haptic rendering algorithm provides dual-channel force feedback incorporating both me-  
117 chanical tissue resistance and thermal effects during electrocautery. The simulation envi-  
118 ronment, developed using iMSTK [15], features detailed anatomical models including the  
119 IMA, surrounding connective tissues, and a beating heart model to recreate the challeng-  
120 ing surgical field conditions. This comprehensive platform allows surgeons to practice  
121 critical technical skills for robotic IMA harvesting in a risk-free virtual environment.



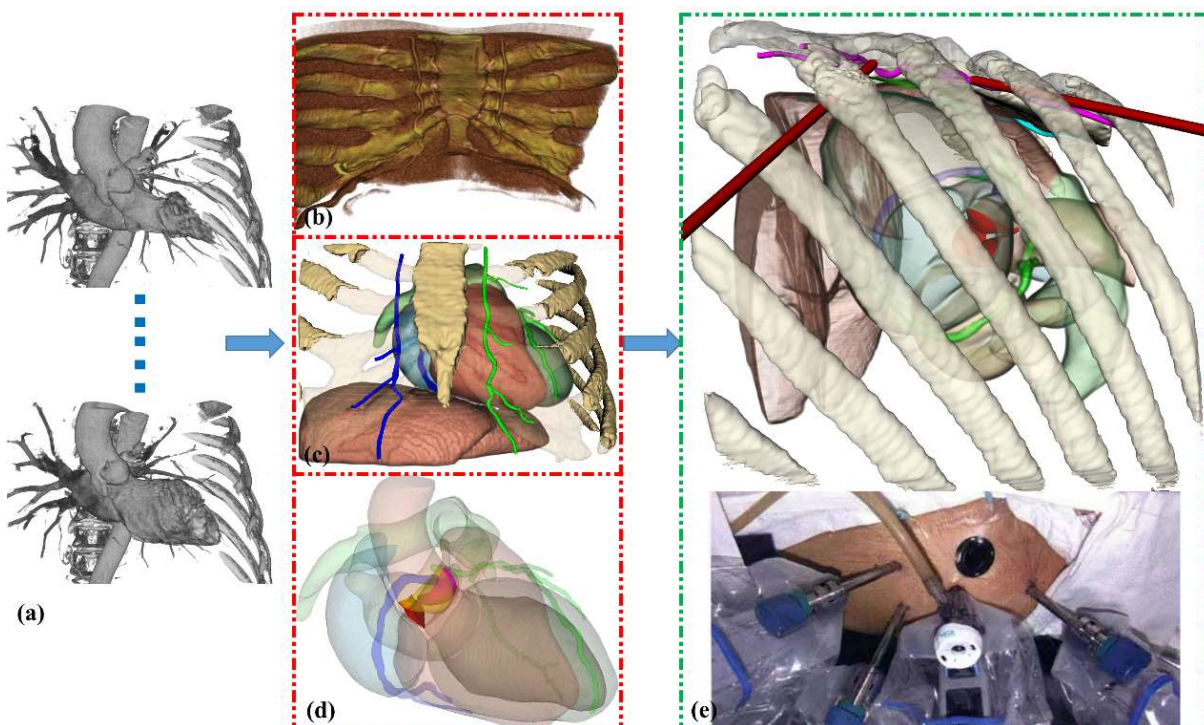
**Figure 1.** Hardware configuration of the proposed virtual surgical simulation platform. The interface consists of two haptic devices, foot pedals for electrocautery activation, and a high-resolution display for surgical scene visualization.

### 2.1. Surgical Anatomy and Motion Constraints

The anatomical layering of the anterior chest wall demonstrates a clear superior-to-deep arrangement, where the superficial fascia forms a membranous layer of connective tissue immediately deep to the dermis, containing collagen, elastic fibers, and neurovascular structures. Deep to this lies the subcutaneous fat, composed of adipose and loose connective tissue with small blood vessels. The IMA are situated much deeper, typically 2-3 cm lateral to the sternum, running vertically behind the costal cartilages and deep to the pectoralis minor muscle. These vessels course between the pleura and internal intercostal muscles within the parasternal region, demonstrating the significant depth at which they reside compared to the more superficial fascial and adipose layers. It is noteworthy that since the internal mammary artery is located on the inner thoracic wall, its anatomical position is adjacent to the constantly beating heart. The periodic motion of the heart is transmitted through the thoracic cavity to the surgical area, significantly limiting the operating space. Particularly during left internal mammary artery harvesting, the cardiac pulsation directly affects the precise control of surgical instruments, which is one of the key factors contributing to the technical difficulty of this procedure. Therefore, when constructing virtual simulation scenarios, it is necessary to consider not only the anatomical relationships of various tissue layers but also simulate the impact of cardiac pulsation on the surgical area to more realistically reproduce the characteristics of the surgical environment.

### 2.2. Images and Processing

147 Cardiac CT imaging was performed using a Revolution Apex scanner (GE Healthcare,  
 148 Milwaukee, WI, USA) during end-expiratory breath-hold with the patient in normal sinus  
 149 rhythm. Image reconstruction was conducted across 11 temporal phases of the cardiac  
 150 cycle, spanning from -5% to 106% of the R-R interval. The acquisition parameters included  
 151 an isotropic slice thickness and increment of 0.625 mm, with an in-plane spatial resolution  
 152 of  $0.23 \times 0.23$  mm. The mean effective radiation dose, calculated in accordance with Euro-  
 153 pean Guidelines for Quality Criteria for Computed Tomography, was 10.49 mSv. Our  
 154 methodological approach was implemented using MONAI (18) framework through the  
 155 Auto3DSeg pipeline. Initial segmentation and reconstruction of the skeletal structures  
 156 (ribs, vertebrae, sternum), diaphragm, and internal mammary artery were performed on  
 157 end-diastolic phase (70%) CT images. Subsequently, HeartDeformNet (19) was employed  
 158 for automated multi-chamber cardiac segmentation, including the left and right ventricles,  
 159 left and right atria, LV myocardium, aorta, and pulmonary artery across all cardiac phases.  
 160 Coronary artery segmentation was performed on the 70% phase images using SimVascu-  
 161 lar-v2023.03.27 (20), where an experienced cardiologist delineated arterial contours on  
 162 cross-sectional planes perpendicular to the vessel centerlines. The dynamic model was  
 163 completed by registering nine cardiac phases (10–90%) to the reference 70% phase, deriv-  
 164 ing transformation matrices for the 3D surface model points of coronary arteries. These  
 165 derived transformation matrices enabled the reconstruction of time-resolved (4D) ana-  
 166 tomical structures throughout the complete cardiac cycle (Fig. 2).



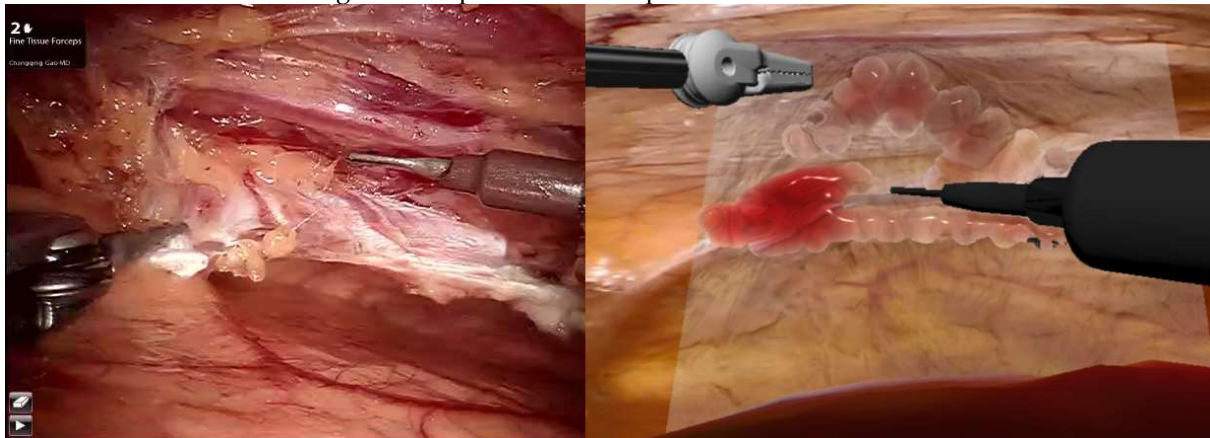
167 **Figure 2.** Visualization of key anatomical structures and surgical setup for robotic CABG. (a) ECG-  
 168 gated sequential images. (b) thoracic cage and diaphragm. (c) internal mammary artery. (d) whole-  
 169 heart mesh incorporating coronary arterial system and aortic valve anatomy. (e) 3D visualization of  
 170 robotic CABG surgical scene showing optimal port placement configuration, including camera port,  
 171 instrument ports and assistant port positions on the left chest wall.  
 172

### 173 2.3. Biomechanical Framework for Dynamic Thoracic Wall Simulation

174 A novel haptic-enabled surgical simulator was developed for robotic-assisted CABG  
 175 procedures. Figure 3 illustrates the parallel comparison between clinical robotic CABG

176  
177

operations and the virtual surgical environment, highlighting the correlation between real-world surgical manipulation and haptic-rendered simulation scenarios.



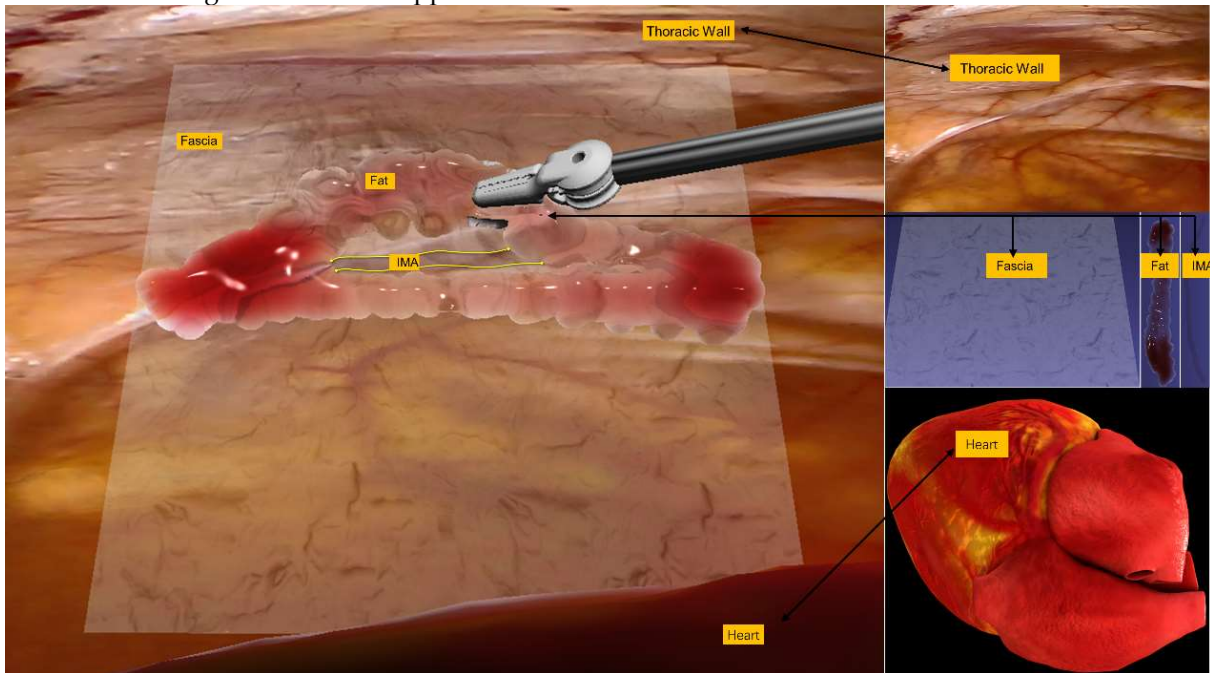
178

179

**Figure 3.** Comparison between real surgical procedure and virtual surgical simulation.

180  
181  
182  
183  
184  
185  
186  
187  
188  
189

To achieve realistic surgical interaction, we present a comprehensive biomechanical simulation framework for thoracic wall tissues, as shown in Figure 4, incorporating four primary anatomical components: fascia superficialis, IMA, subcutaneous adipose tissue and dynamic heart. The system employs a multi-resolution approach with distance and dihedral angle constraints to model tissue mechanics. The fascia and IMA are simulated using triangular mesh discretization, while the subcutaneous fat is represented through a connective tissue strand network. A bidirectional coupling mechanism enables real-time deformation propagation between tissues, optimized for computational efficiency while maintaining anatomical accuracy. This framework is specifically designed for real-time surgical simulation applications.

190  
191  
192  
193  
194

**Figure 4.** Multi-tissue biomechanical simulation framework of thoracic wall. The framework incorporates four anatomical components (fascia superficialis, IMA, subcutaneous adipose tissue, and beating heart), utilizing multi-resolution mesh discretization and tissue coupling mechanisms for real-time surgical simulation.

195

### 2.3.1. Fascia Superficialis Simulation

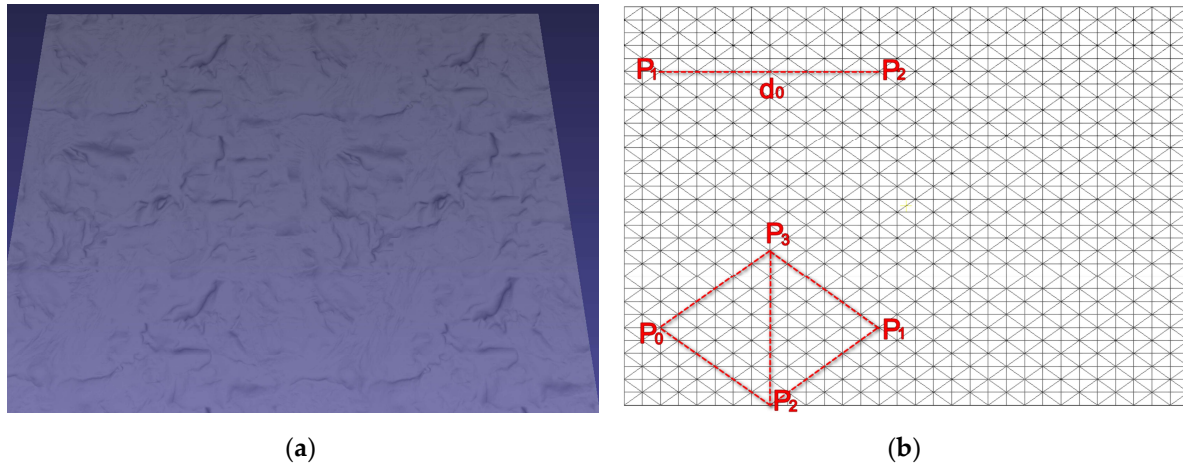


**Figure 5.** Fascia superficialis discretization and constraint mechanisms. (a) Triangular mesh representation of fascia superficialis, where vertices encode tissue surface geometry and faces define the connectivity structure. (b) Biomechanical constraints governing tissue deformation: distance preservation constraint maintains structural integrity, while dihedral angle constraint controls bending behavior.

The fascia superficialis simulation framework is based on PBD, employing a triangular mesh discretization  $M = (V, F)$  on a rectangular domain  $D = [0, \omega] \times [0, h]$  (Fig. 5a), where  $V = \{v_i\}_{i=1}^n \subset \mathbb{R}^3$  represents the set of vertex positions and  $F = \{f_j\}_{j=1}^m \subset \mathbb{N}^3$  denotes the set of triangular faces defining the mesh connectivity. The dynamics are governed by a two-stage solver incorporating position updates and constraint satisfaction. For each vertex  $i$ , the position  $x_i^*$  is initially predicted as:

$$x_i^* = x_i(t) + v_i(t)\Delta t + \frac{1}{2}a_{ext}\Delta t^2 \quad (1)$$

where  $x_i(t)$  is the current position at time  $t$ ,  $v_i(t)$  denotes the velocity at time  $t$ ,  $\Delta t$  is the time step size,  $a_{ext}$  represents external acceleration, primarily gravity. The system is constrained by two primary mechanisms reflecting the biomechanical properties of fascia superficialis: distance preservation constraint and dihedral angle constraint (Fig. 5b). The tissue's tensile resistance is modeled through a distance preservation constraint:

$$C_d(p_1, p_2) = |p_1 - p_2| - d_0 = 0 \quad (2)$$

where  $d_0$  represents the rest length between particle pairs  $p_1$  and  $p_2$ . This constraint ensures the maintenance of structural integrity by preserving inter-particle distances during deformation. The dihedral angle constraint  $C_\theta$  operates on four vertices  $p_0, p_1, p_2, p_3$  forming adjacent triangles with a shared edge  $p_2p_3$ .

$$C_\theta(p_1, p_2, p_3, p_4) = \text{atan2}(n_1 \times n_2 \cdot (p_3 - p_2), |p_3 - p_2| \cdot n_1 \cdot n_2) - \theta_{rest} \quad (3)$$

where  $\text{atan2}(y, x)$  returns the angle  $\theta \in [-\pi, \pi]$  such that  $x = r \cos \theta$  and  $y = r \sin \theta$  for some  $r > 0$ .  $n_1 = \frac{(p_2 - p_0) \times (p_3 - p_0)}{|(p_2 - p_0) \times (p_3 - p_0)|'}$ ,  $n_2 = \frac{(p_3 - p_1) \times (p_2 - p_1)}{|(p_3 - p_1) \times (p_2 - p_1)|'}$ ,  $\theta_{rest}$  denotes the initial dihedral angle measured in the rest configuration of the mesh, serving as the reference state for the bending constraint.

These constraints are iteratively satisfied through position corrections  $\Delta x = \lambda \nabla C$ , where  $\lambda = -\frac{c(x)}{|\nabla C(x)|^2}$ . The system incorporates both linear damping force  $F_d$  and angular damping force  $T_d$  to simulate the viscoelastic properties of fascial tissue.

$$\begin{cases} F_d = -k_l v & k_l = 0.03 \text{ kg/s} \\ T_d = -k_c \omega & k_c = 0.01 \text{ kg} \cdot m^2/s \end{cases} \quad (4)$$

where  $v$  is the linear velocity and  $\omega$  is the angular velocity of the particles. The numerical integration employs a time step of  $\Delta t = 5\text{ms}$  with 5 solver iterations per step, ensuring stable and anatomically plausible deformation behavior. Boundary conditions are enforced by fixing perimeter vertices, while uniform mass distribution is applied across all vertices. This formulation provides a robust balance between computational efficiency and physiological accuracy, making it particularly suitable for real-time surgical simulation applications involving fascial tissue manipulation.

### 2.3.2. Multi-resolution IMA Vessel Simulation

Similar to the fascia model, the IMA vessel's mechanical behavior is governed by a dual-constraint system: a distance preservation constraint with high stiffness coefficient to maintain vessel wall integrity, and a dihedral angle constraint with lower stiffness to model the characteristic bending behavior of vascular structures. The simulation employs a multi-resolution approach, utilizing a low-resolution mesh for physical computations (Fig. 6b) and a high-resolution mesh for visualization (Fig. 6c), optimizing both computational efficiency and visual fidelity. The system employs uniform mass distribution across all vertices of the simulation mesh and notably operates in a gravity-free environment to simulate the in-situ mechanical conditions of the thoracic cavity.

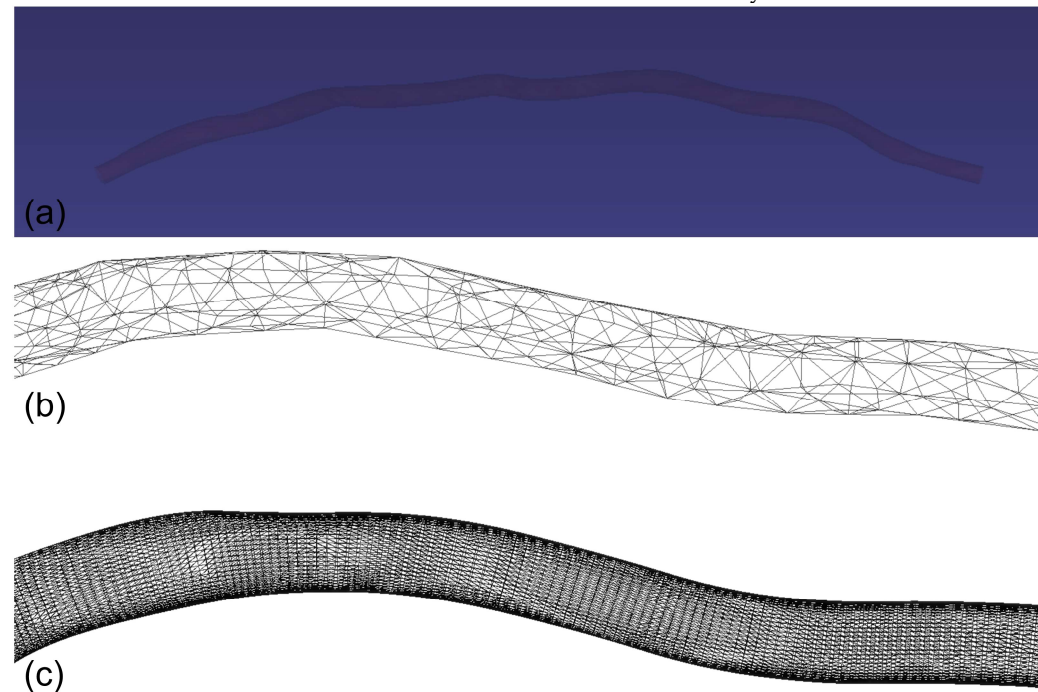


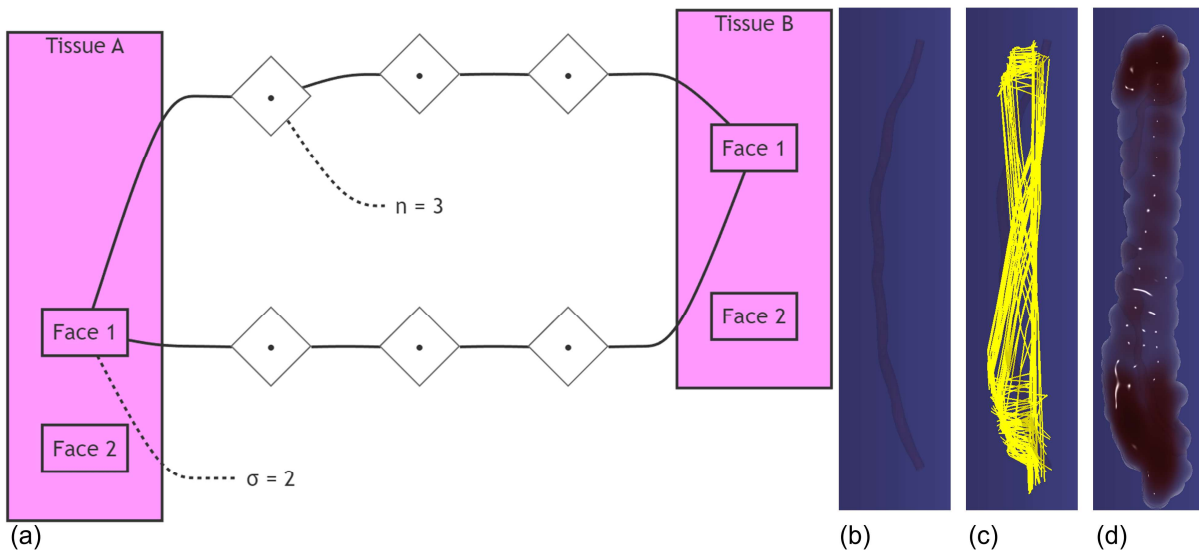
**Figure 6.** Multi-resolution representation of the Internal Mammary Artery (IMA). (a) IMA visualization in the virtual surgical environment demonstrating anatomically accurate vessel positioning and appearance. (b) Low-resolution simulation mesh optimized for efficient physical computation. (c) High-resolution visualization mesh providing enhanced geometric detail.

The numerical framework utilizes position updates of the form  $x_i^* = x_i(t) + v_i(t)\Delta t$  for each vertex  $i$  with constraint satisfaction achieved through iterative position corrections, where  $x_i^*$  represents the predicted position of vertex,  $x_i(t)$  is the current position at time  $t$ ,  $v_i(t)$  denotes the velocity at time  $t$ ,  $\Delta t$  is the time step size. The high-resolution display mesh is subsequently updated through linear interpolation based on the deformed simulation mesh. This formulation provides a biomechanically plausible representation of IMA deformation during surgical manipulation, with particular emphasis on maintaining vessel wall integrity while allowing for natural flexion and torsion. The model's high-resolution geometric fidelity, combined with its physically-based deformation

characteristics and computationally efficient multi-resolution architecture, makes it especially suitable for surgical simulation applications involving thoracic vessel manipulation.

254  
255  
256

### 2.3.4. Connective Tissue Modeling



257

258  
259  
260  
261  
262  
263  
264

**Figure 7.** Multi-component system for IMA connective tissue modeling. (a) Parameterization of connective tissue strands. The density of connections between tissues is controlled by two key parameters:  $\sigma$  (strands per face) and  $n$  (segments per strand). In this example,  $\sigma = 2$  strands emanate from Face 1 of Tissue A, and each strand is subdivided into  $n = 3$  segments, creating a network of connection points ( $\bullet$ ) between the tissues. This parameterization enables precise control over both the density of connections and the granularity of deformation simulation. (b) A low-resolution IMA mesh. (c) Connective tissue strand network. (d) Physically-based connective tissue model with SPH.

265  
266  
267  
268  
269

To simulate the physical interaction between the IMA and subcutaneous fat tissue, we established a PBD model with connective tissue strands. The system consists of three main components: a low-resolution IMA mesh, a cylindrical support structure representing the thoracic wall, and interconnecting strands. The IMA and support structure are modeled as static PBD objects with uniform mass distribution:

$$m_v = \frac{M_{total}}{N_v} \quad (5)$$

270  
271  
272  
273  
274

where  $m_v$  represents the mass of each vertex,  $M_{total}$  is the total mass, and  $N_v$  is the number of vertices in the mesh. The connective tissue is represented by a network of strands generated between proximal surfaces, governed by the proximity condition:  $d_{ij} \leq d_{max}$ , where  $d_{ij}$  is the distance between surface elements  $i$  and  $j$ , and  $d_{max}$  is either explicitly specified or automatically calculated as the distance between object centers:

$$d_{max} = \|C_A - C_B\| \quad (6)$$

275  
276  
277

Subsequently, the total motion disparity  $M(t)$  at each cardiac phase  $t$  was computed by integrating the normalized displacement differences across all corresponding EAT-pericardium point pairs within the defined ROI:

$$M(t) = \sum_{p \in \Omega_{ROI}^t} \|\hat{D}_{diff}(p, q, t)\|_2 \quad (7)$$

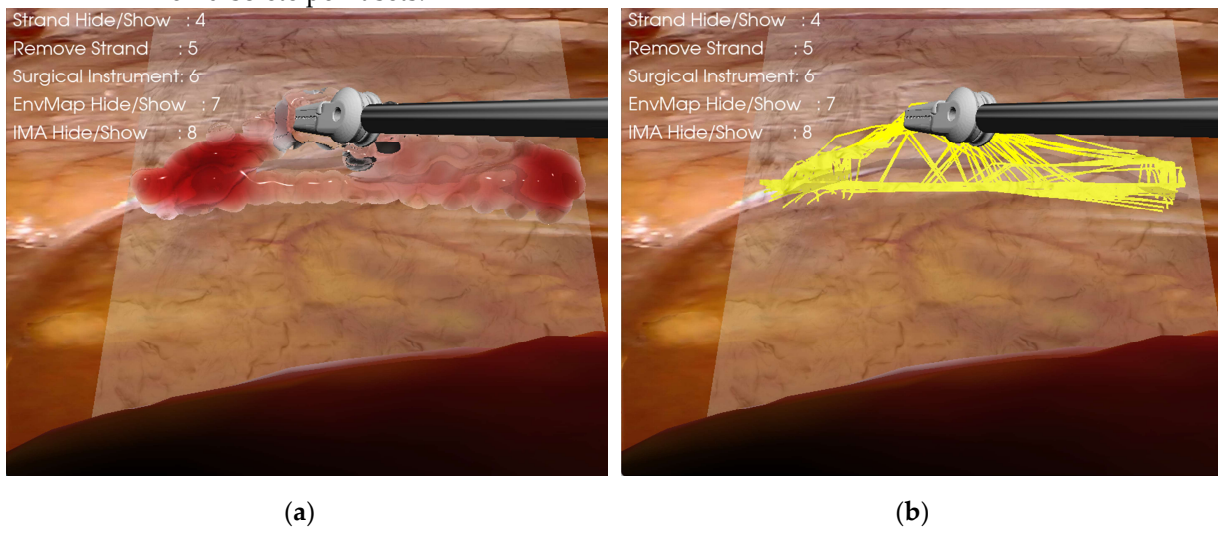
278  
279  
280  
281  
282

where  $C_A$  and  $C_B$  represent the centers of the IMA and support structure respectively. The density of connections is controlled by two parameters: strands per face  $\sigma$  and segments per strand  $n$  (Fig. 7a). The strands follow the surface normal directions within an allowed angle deviation  $\theta$ , creating a physically plausible representation of the connective tissue structure (Fig. 7c). Each strand is subject to distance constraints and implements

283  
284 SPH-based (Smoothed Particle Hydrodynamics) interactions to simulate the viscoelastic  
285 behavior of the biological tissue (Fig. 7d). This model provides a balanced approach be-  
286 tween computational efficiency and physical accuracy, suitable for surgical simulation ap-  
287 plications where real-time performance is crucial.

### 288 2.3.3. Bidirectional Coupling of IMA and Adipose Tissue

289 As shown in Figure 8, we implemented a dynamic coupling mechanism between the  
290 IMA and surrounding adipose tissue, utilizing a real-time deformation propagation sys-  
291 tem. The coupling is achieved through a bidirectional force transfer model that operates  
on discrete point sets.



292 **Figure 8.** Biomechanical coupling visualization in soft tissue manipulation. (a) Visualization of cou-  
293 pled tissue dynamics. Forceps grasping of the fascia superficialis results in concurrent elevation of  
294 the adherent subcutaneous fat, demonstrating the biomechanical coupling between tissue layers. (b)  
295 Deformation mapping mechanism between fascia superficialis and adjacent connective tissue  
296 strands.

297 The deformation mapping between the IMA and connective tissue strands is gov-  
298 erned by:

$$O_{l,i} = \hat{O}_{ima,j} \cdot \min(|O_{ima,j}|, \lambda_{max}) \quad (8)$$

299 where  $O_{l,i}$  is the offset of the i-th point in the connective tissue line mesh,  $O_{ima,j}$  is the  
300 offset of the corresponding j-th point in the IMA mesh,  $\hat{O}_{ima,j}$  represents the normalized  
301 direction vector,  $\lambda_{max}$  is the maximum allowed deformation magnitude.

302 For the inverse coupling from adipose tissue to IMA, the deformation transfer is de-  
303 scribed by:

$$O_{ima,i} = \begin{cases} \hat{O}_{fat,j} \cdot \min(|O_{fat,j}|, \lambda_{max}) & \text{for } \beta=1 \\ 0.8 \cdot O_{ima,i} & \text{for } \beta=0 \end{cases} \quad (9)$$

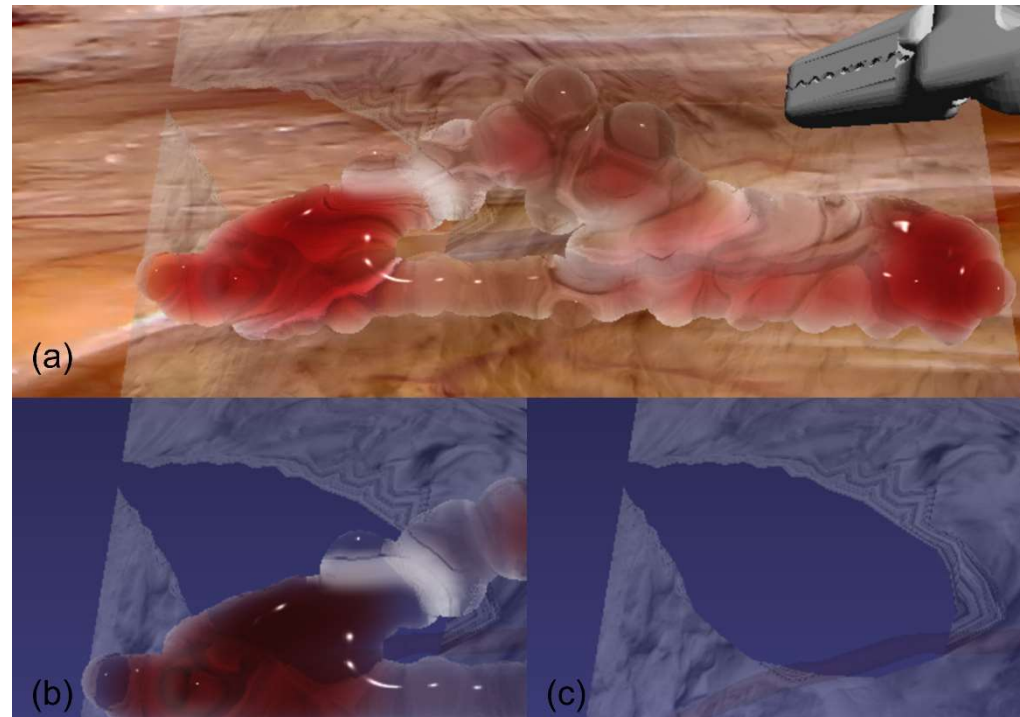
304 where  $O_{fat,j}$  represents the offset of the corresponding fat tissue point, and  $\beta \in \{0,1\}$   
305 serves as the coupling state indicator. This bidirectional coupling mechanism ensures  
306 physically plausible deformation behavior while maintaining computational efficiency  
307 through parallel processing. The damping coefficient of 0.8 in the non-coupled state ( $\beta=0$ )  
308 prevents unrealistic oscillations and provides smooth motion decay. To optimize runtime  
309 performance, the vertex coupling relationships are pre-computed and stored in mapping  
310 arrays, eliminating the need for costly spatial queries during simulation. This approach  
311 significantly enhances computational efficiency while maintaining physical accuracy in  
312 the deformation propagation process.

313  
314  
315  
316  
317  
318  
319  
320  
321  
322  
323

#### 2.4. Interactive Haptic-enabled Surgical Manipulation and Cutting

This section presents a comprehensive framework for surgical interaction modeling, encompassing four key components: (1) a topology-preserving cutting method for fascia superficialis simulation using dynamic mesh modification; (2) a geometric intersection-based algorithm for connective tissue cutting within adipose structures; (3) a precise kinematic model for surgical instrument motion control, particularly focusing on forceps manipulation; and (4) a dual-channel haptic feedback system for electrocautery simulation with thermal effects. These components collectively enable realistic surgical tissue manipulation and cutting operations while maintaining computational efficiency for real-time performance.

##### 2.4.1. Topology-Preserving Cutting Method



324

**Figure 9.** Topological modification scheme for fascia superficialis cutting simulation. (a) Complete surgical scene showing the integrated fascia superficialis cutting simulation with all anatomical components. (b) Magnified view of the cutting region with chest wall model hidden, highlighting the interaction between fascia superficialis and surrounding tissues. (c) Further magnified view with adipose tissue hidden, demonstrating the detailed fascia superficialis structure and cutting dynamics.

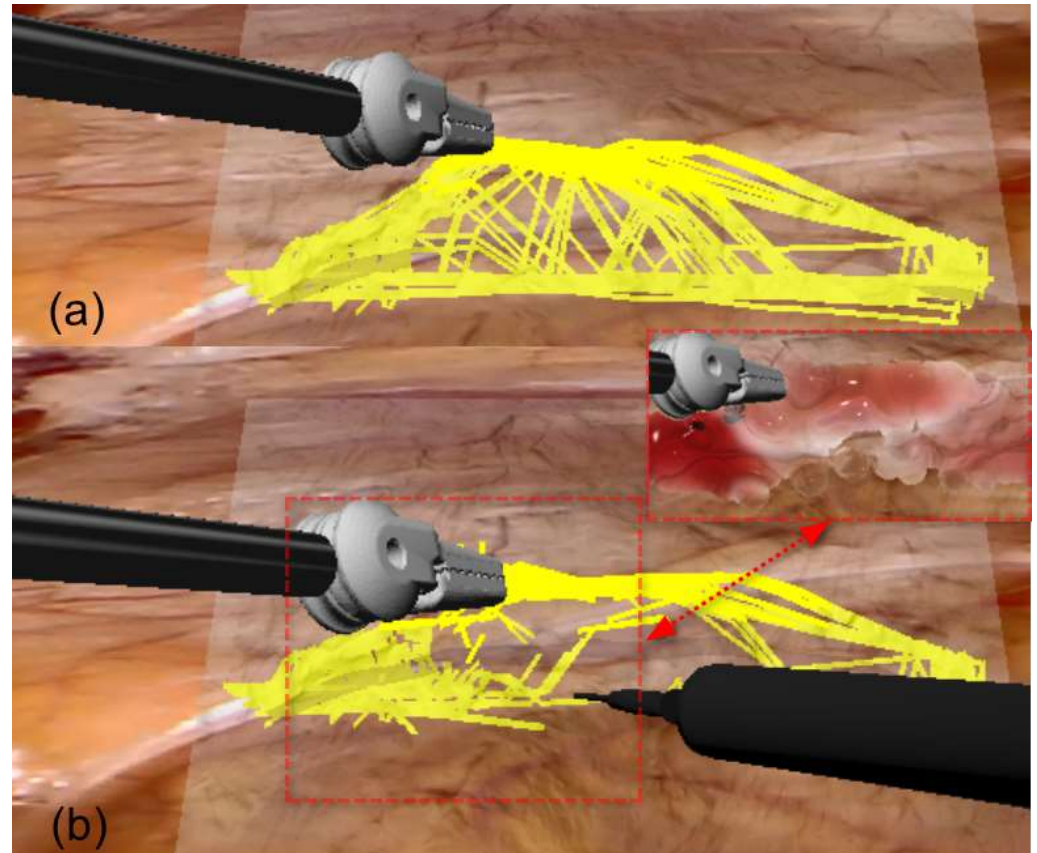
331  
332  
333  
334  
335  
336  
337  
338  
339  
340  
341  
342

As shown in Figure 9, we present a cutting algorithm that implements a dynamic topological modification scheme within the PBD framework, specifically designed for fascia superficialis simulation. Given an input mesh  $M = (V, E)$  and a cutting geometry  $G_c$  with proximity threshold  $\epsilon$ , where  $V = \{v_i\}_{i=1}^n \subset \mathbb{R}^3$  denotes the set of vertex positions, with  $n$  being the total number of vertices.  $E = \{e_k\}_{k=1}^m \subset \mathbb{N}^2$  represents the set of edges, where each edge  $e_k = (i, j)$  connects vertices  $v_i$  and  $v_j$ . The algorithm first identifies vertices within the cutting zone by computing signed distances  $d_i = dist(v_i, G_c)$  where  $|d_i| < \epsilon$ . The mesh undergoes local remeshing to generate new vertices  $V_{new}$  and modified connectivity  $E_{new}$ , resulting in an updated mesh  $M_{new} = (V \cup V_{new}, E_{new})$ . The system maintains constraint coherence through explicit tracking of removed and added constraint sets, while simultaneously propagating both current vertex positions  $x_i(t) \rightarrow x'_i(t)$  and reference configurations  $x_i^0 \rightarrow (x_i^0)'$ . This approach ensures geometric consistency

343  
344  
345

and physical plausibility while supporting real-time performance through efficient constraint management.

#### 2.4.2. Connective tissue surgical cutting simulation



346

347  
348  
349  
350  
351

**Figure 10.** Illustration of our proposed cutting approach for deformable adipose tissue simulation. (a) Initial configuration of connective tissue strands before cutting, showing the natural structural arrangement within adipose tissue. (b) Post-cutting state of connective tissue strands with corresponding adipose tissue structure shown in the upper right inset, demonstrating the geometric intersection-based removal algorithm's effect on tissue architecture.

352  
353  
354

As shown in Figure 10, we propose a novel connective tissue surgical cutting approach that implements a geometric intersection-based removal algorithm for deformable adipose tissue. The cutting plane  $P$  is defined as:

$$\{x \in \mathbb{R}^3 : n \cdot (x - p) = 0\} \quad (10)$$

355  
356  
357  
358  
359

where  $p$  represents the surgical tool's position vector and  $n$  denotes the unit normal vector derived from tool orientation. The tool's orientation is characterized by an orthonormal basis  $\{n, l, f\}$ , with  $n = R \cdot (0, 1, 0)^T$ ,  $l = R \cdot (1, 0, 0)^T$ , and  $f = R \cdot (0, 0, 1)^T$ , where  $R \in SO(3)$  is the rotation matrix of the surgical tool. The connective tissue structure is discretized as a set of line segments:

$$S = \{s_i\}_{i=1}^N \quad (11)$$

360  
361

where each segment  $s_i = \{(1 - t)v_i^0 + tv_i^1 : t \in [0, 1]\}$  is defined by endpoint vertices  $v_i^0, v_i^1 \in \mathbb{R}^3$ . A fascial segment is marked for removal when it satisfies:

$$\exists x \in s_i : |l \cdot (x - p)| < \frac{\omega}{2} \wedge |f \cdot (x - p)| < \frac{\omega}{2} \wedge n \cdot (x - p) = 0 \quad (12)$$

362  
363

where  $\omega$  represents the cutting width. The visual representation of the connective tissue undergoes a continuous transformation following

$$d_{t+1} = 0.96d_t \quad (13)$$

where  $d_t$  represents the particle diameter at time  $t$ , terminating visibility when  $d_t < 6 \times 10^{-4}$  to simulate the gradual dissection of fascial layers. This methodology, implemented through PBD with parallel processing and SPH visualization, provides a computationally efficient approach for connective tissue dissection simulation while maintaining physical plausibility and visual fidelity, demonstrating robust handling of topological changes and real-time performance suitable for surgical training applications.

#### 2.4.3. Kinematic Modeling of Surgical Instrument Motion

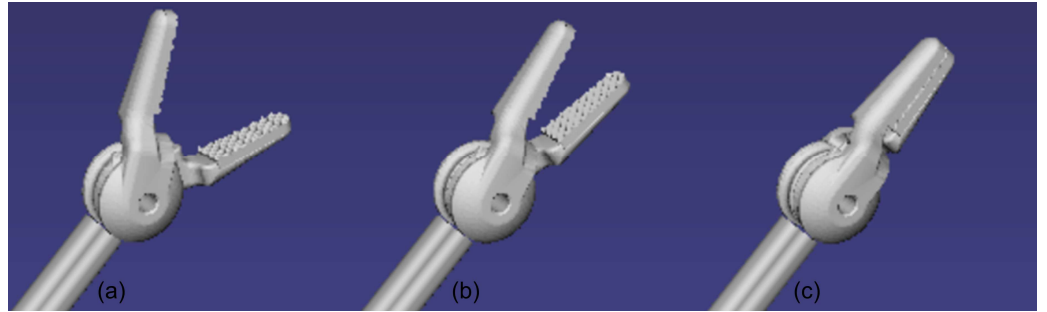


**Figure 11.** Progressive closure sequence of a DeBakey forceps. (a) Maximum opening angle ( $30^\circ$ ). (b) Half-closed position ( $15^\circ$ ). (c) Complete closure ( $0^\circ$ ).

As shown in Figure 11, the surgical instrument can be mathematically modeled as a kinematic chain operating in the configuration space:

$$Q = SE(3) \times [-\theta_{max}, \theta_{max}]^2 \quad (14)$$

where  $SE(3)$  represents the Special Euclidean group in 3D space, describing the 6-DOF pose of the tool.  $\theta_{max}$  is the maximum jaw opening angle, typically set to  $30^\circ$  (Fig. 11a). The tool's world position is governed by the transform hierarchy:

$$T_{world} = T_{controller} \cdot T_{local} \cdot T_{initial} \quad (15)$$

where  $T_{controller}$  is the controller's transformation matrix,  $T_{local}$  is the local joint transformation matrix,  $T_{initial}$  is the initial offset transformation matrix. The jaw motion follows a time-dependent angular control model:

$$\theta(t + dt) = \theta(t) + \dot{\theta} \cdot dt \quad (16)$$

where  $\theta(t)$  is the jaw angle at time  $t$ ,  $\dot{\theta}$  is the angular velocity determined by button inputs,  $dt$  is the time step. The upper and lower jaws rotate symmetrically around axis  $\vec{\alpha}$  according to:  $T_{upper} = R(\theta, \vec{\alpha})$ ,  $T_{lower} = R(-\theta, \vec{\alpha})$ , where  $\vec{\alpha}$  is the rotation axis vector of the jaw hinge. The system transitions between open and closed states based on a threshold angle of  $2.86^\circ$ , considering closed when below this value. Both visual and collision geometries are updated through the transform chain. This framework ensures precise control and realistic simulation of the surgical tool's kinematics during minimally invasive procedures.

#### 2.4.4. Force Feedback Modeling for Electrosurgical Simulation



**Figure 12.** Physical and Virtual Electrotomy Tool for Robotic Cardiac Surgery. (a) Dual-view photographs of the actual electrocautery instrument. (b) 3D virtual model of the electrocautery tool.

As a critical component of our robotic CABG simulation platform, we implemented a haptic-enabled electrocautery module (Fig. 12) that integrates real-time force feedback rendering with tissue deformation modeling. This module employs a sophisticated dual-channel force feedback algorithm that decomposes tool-tissue interaction forces into two components: the primary channel models perpendicular tissue resistance force

$$F_n = k_d * d + c_d * v_n, \quad 0 \leq F_n \leq 5N \quad (17)$$

where  $k_d$  represents tissue stiffness coefficient,  $d$  denotes penetration depth,  $c_d$  is the damping coefficient, and  $v_n$  indicates normal velocity vector; while the secondary channel simulates lateral cutting resistance through

$$F_t = \mu * F_n + k_c * v_t, \quad 0 \leq F_t \leq 2N \quad (18)$$

where  $\mu$  represents dynamic friction coefficient,  $k_c$  denotes cutting resistance coefficient, and  $v_t$  indicates tangential velocity vector. The total force feedback  $F_{total} = F_n + F_t + F_{therm}$  incorporates additional thermal modulation based on power settings and tissue properties. The thermal force component  $F_{therm}$  represents a force feedback modulation term that simulates tissue response changes due to electrosurgical thermal effects. It is mathematically expressed as

$$F_{thermal} = k_t * P * e^{-\alpha d} \quad (19)$$

where  $k_t$  is the thermal coefficient specific to tissue type,  $P$  represents the electrosurgical power setting (typically 30-50W),  $\alpha$  is the thermal decay coefficient, and  $d$  denotes the thermal effect depth. This force component captures several critical aspects of electrosurgical procedures: tissue carbonization resistance changes, cutting/coagulation effects at different power settings, mechanical property alterations due to thermal diffusion, and tissue stiffness variations caused by moisture evaporation. Real-time tissue response is computed using a multi-resolution mesh model, incorporating both elastic deformation and thermal diffusion properties. The force profile varies according to different tissue layers and operational modes (cutting vs. coagulation), with haptic rendering updated at 1000Hz to ensure stable force feedback, while visual feedback maintains a minimum refresh rate of 60Hz. This comprehensive electrocautery simulation module

enables surgical trainees to practice specific electrocautery techniques with realistic tactile sensation and visual feedback, accurately representing various surgical maneuvers including initial tissue puncture, depth-dependent cutting resistance, and layer-specific mechanical properties.

### 3. Results

The experiment was designed to evaluate the impact of cardiac motion on surgical performance during IMA harvesting using our virtual simulation platform. The simulation scenarios were configured with identical anatomical structures but different cardiac motion states: one with realistic cardiac motion (dynamic group) and one with a static heart (static group).

A standardized surgical task was defined as harvesting a 10-cm segment of the left IMA using virtual robotic instruments. The surgical workflow followed clinical protocols, including initial exposure, vessel identification, and careful dissection along the IMA course. The virtual surgical instruments were modeled based on the da Vinci surgical system's EndoWrist instruments. A single experienced operator (>100 cases of CABG) performed 10 repetitions for each scenario in randomized order to minimize learning effects. A mandatory 15-minute rest period was implemented between trials to reduce operator fatigue. Before formal trials, the operator underwent a standardized training session to achieve stable performance in the virtual environment. All experiments were conducted using the same hardware setup: a workstation equipped with an NVIDIA RTX 4080GPU, Intel i7-13700HK CPU, and 32GB RAM, ensuring consistent computational performance throughout the trials.

Here we propose a novel Spatial Asymmetry Index (SAI) to quantitatively evaluate the spatial distribution characteristics of surgical tool trajectories during IMA harvesting. The SAI is mathematically defined as:

$$SAI = \frac{1}{n} \sum_{i=1}^n \frac{d_i}{R} \cdot sign(d_i) \quad (20)$$

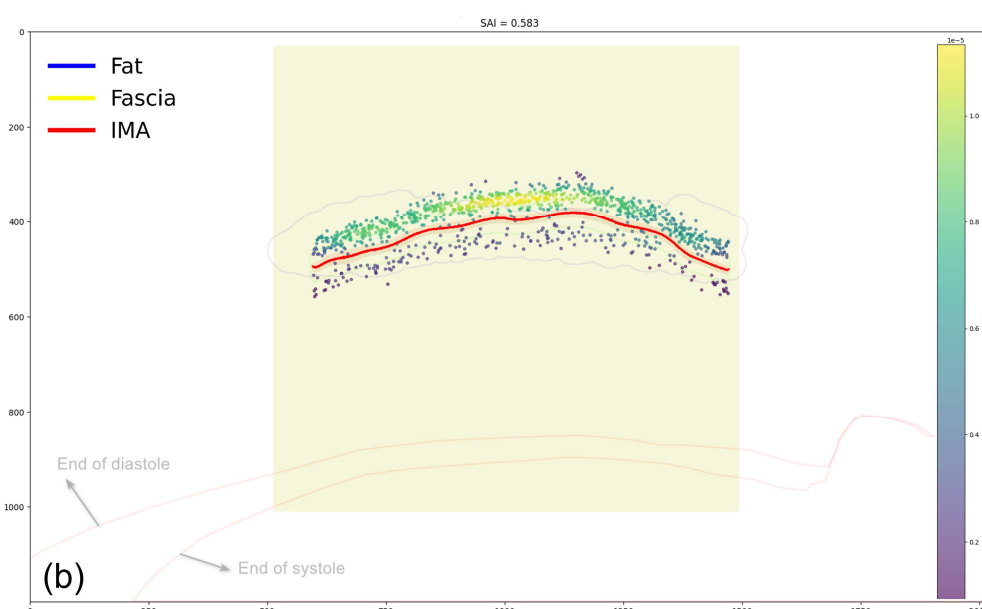
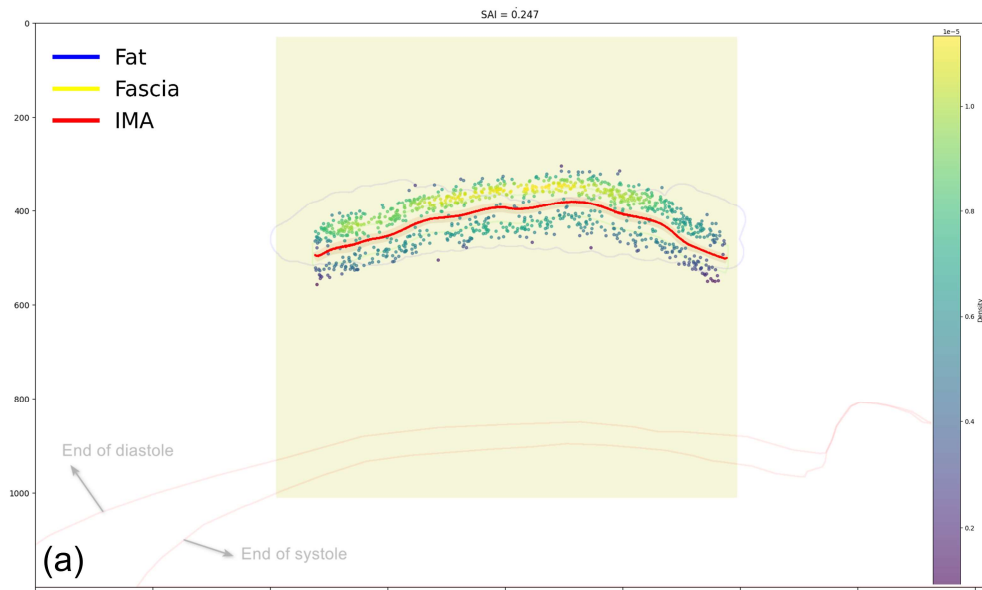
where  $d_i$  represents the perpendicular distance from the tool position to the IMA centerline,  $R$  denotes a standardized reference distance (2mm safety zone radius), and  $sign(d_i)$  indicates the directional component (negative for cardiac side, positive for non-cardiac side), and  $n$  represents the total number of sampling points recorded at 60Hz during the procedure. This metric effectively captures the spatial bias in surgical manipulation, with positive SAI values indicating a preference for operating on the side away from the heart, while values approaching zero suggest more symmetric distribution.

**Table 1.** Comparison of SAI between Dynamic and Static Groups.

Trial No.	Dynamic Group SAI	Static Group SAI
1	0.583	0.247
2	0.621	0.268
3	0.545	0.221
4	0.602	0.285
5	0.568	0.238
6	0.634	0.276
7	0.592	0.212
8	0.551	0.257
9	0.615	0.228

10	0. 577	0. 243
<b>Mean±SD</b>	$0.589 \pm 0.029$	$0.248 \pm 0.024$

As shown in Table 1, statistical analysis revealed significantly higher SAI values in the dynamic group compared to the static group ( $0.589 \pm 0.029$  vs  $0.248 \pm 0.024$ ,  $p < 0.001$ ), demonstrating that surgeons systematically adjusted their manipulation strategies to compensate for cardiac motion by maintaining safer working distances from the beating heart. This behavioral adaptation was further validated through spatial density heat maps, which showed distinct clustering of tool positions on the non-cardiac side in the dynamic group (SAI consistently above 0.5), whereas the static group exhibited a more balanced but still slightly asymmetric distribution along the IMA centerline (SAI values around 0.25). As illustrated in Figure 13, the 3D anatomical structures (Fascia, subcutaneous fat tissue, and IMA) and the corresponding tool trajectory data during IMA dissection were projected orthogonally onto a 2D visualization plane for comparative analysis. The SAI thus provides a robust quantitative measure for assessing how cardiac motion influences surgical approach and spatial decision-making during robotic IMA harvesting procedures, with the substantial difference in *SAI* values (mean difference = 0.341) indicating a clear adaptation of surgical strategy in response to cardiac motion.



469  
470  
471  
472  
473  
474

**Figure 13.** Representative images showing tool position distributions during IMA dissection. Each heatmap incorporates anatomical structures, IMA centerline trajectory (red), and a density-based color gradient representing the frequency of tool positions. (a) Representative image from the Static Group ( $SAI = 0.247$ ) showing balanced but slightly asymmetric distribution of tool positions along the IMA centerline. (b) Representative image from the Dynamic Group ( $SAI = 0.583$ ) demonstrating distinct clustering of tool positions on the non-cardiac side.

#### 475 4. Discussion

476 This study presents a comprehensive virtual simulation framework for robotic internal  
477 mammary artery harvesting, demonstrating several significant advances in surgical  
478 simulation technology. Our organ-active structure modeling method, incorporating func-  
479 tional relationship constraints, demonstrated high anatomical fidelity with sub-millimeter  
480 geometric accuracy. The bidirectional coupling mechanism successfully synchronized  
481 multiple anatomical structures, including the internal mammary artery, fascia, adipose  
482 tissue, and connective tissue, maintaining temporal consistency within  $\delta t \leq 15\text{ms}$ .

483 The topology-preserving cutting algorithm for fascia superficialis demonstrated ro-  
484 bust performance in maintaining mesh integrity during dissection, while the geometric  
485 intersection-based algorithm effectively simulated adipose tissue dissection. Notably, our  
486 dual-channel haptic feedback system achieved a 1kHz update rate, essential for stable  
487 force rendering, while incorporating thermal effects in electrocautery simulation. The sys-  
488 tem maintained consistent performance metrics, including a visual feedback refresh rate  
489 of 60Hz ( $SD \pm 2.5\text{Hz}$ ), ensuring smooth surgical interaction.

490 Quantitative analysis using the SAI revealed significant behavioral adaptations in  
491 surgical technique due to cardiac motion. The dynamic cardiac group demonstrated sig-  
492 nificantly higher SAI values compared to the static group ( $0.589 \pm 0.029$  vs  $0.248 \pm 0.024$ ,  $p <$   
493  $0.001$ ), indicating systematic adjustment of surgical approach to compensate for cardiac  
494 motion. Spatial density analysis further validated this finding, showing distinct clustering  
495 of tool positions on the non-cardiac side in the dynamic group.

##### 496 *Study Limitations*

497 Several limitations of the current system warrant consideration. The model does not  
498 fully account for anatomical variations between patients, and the force feedback models  
499 require further clinical validation. Additionally, the simulation environment lacks certain  
500 surgical complications, such as bleeding events, and system evaluation is based on data  
501 from a single expert operator.

#### 502 5. Conclusions

503 This study presents a novel virtual simulation platform for robotic internal mam-  
504 mary artery harvesting that successfully integrates dynamic anatomical modeling with  
505 real-time haptic feedback. By incorporating cardiac motion effects and implementing  
506 comprehensive tissue interaction mechanisms, our platform provides a realistic training  
507 environment that closely mimics the challenges of actual surgical procedures. Quantita-  
508 tive evaluation demonstrates the system's effectiveness in capturing the essential technical  
509 aspects of IMA harvesting, suggesting its potential value as a training tool for robotic car-  
510 diac surgery. While further validation and refinement are needed, this work establishes a  
511 promising foundation for the development of next-generation surgical simulation systems.

512 **Supplementary Materials:** The following supporting information can be downloaded at:  
513 [www.mdpi.com/xxx/s1](http://www.mdpi.com/xxx/s1); Video S1: title; Video S2: title.

514 **Author Contributions:** Conceptualization, R.W. and T.R.; methodology, S.W. and L.Z.; software,  
515 S.W.; validation, T.R., N.C. and R.W.; formal analysis, S.W.; investigation, T.R.; resources, N.C., R.W.,

S.W. and L.Z.; data curation, T.R. and S.W.; writing—original draft preparation, S.W. and T.R.; writing—review and editing, N.C., R.W. and L.Z.; visualization, S.W.; supervision, N.C., R.W. and L.Z.; funding acquisition, N.C., R.W. and L.Z. All authors have read and agreed to the published version of the manuscript.

**Funding:** This study was funded by the National Natural Science Foundation of China(62031020), National Key R&D Plan(2022YFB4700800), National Natural Science Foundation of China(62476286), Beijing Science and Technology Plan Project(Z231100005923039).

**Institutional Review Board Statement:** The study was conducted in accordance with the Declaration of Helsinki and approved by the Ethics Committee of the General Hospital of the Chinese People's Liberation Army, which accepted this protocol(protocol code: S2024-580).

**Informed Consent Statement:** Informed consent was obtained from all subjects involved in the study.

**Data Availability Statement:** The data used in this study are not publicly available due to privacy and ethical restrictions, as they contain sensitive patient information. Access to the data is restricted to comply with confidentiality agreements and institutional regulations.

**Conflicts of Interest:** The authors declare no conflicts of interest.

## References

1. The top 10 causes of death. Available online: <https://www.who.int/news-room/fact-sheets/detail/the-top-10-causes-of-death> (accessed March 10, 2020).
2. Hemli JM, Patel NC. Robotic Cardiac Surgery. *Surg Clin North Am* 2020;100:219–236. doi:10.1016/j.suc.2019.12.005.
3. Virk HUH, Lakhter V, Ahmed M, O' Murchu B, Chatterjee S. Radial Artery Versus Saphenous Vein Grafts in Coronary Artery Bypass Surgery: a Literature Review. *Curr Cardiol Rep* 2019;21:36. doi:10.1007/s11886-019-1112-1.
4. Bonatti J, Wallner S, Winkler B, Grabenwöger M. Robotic totally endoscopic coronary artery bypass grafting: current status and future prospects. *Expert Rev Med Devices* 2020;17:33–40. doi:10.1080/17434440.2020.1704252.
5. Balkhy HH, Nathan S, Torregrossa G, et al. The learning curve of robotic totally endoscopic coronary bypass: insights from a single-center experience. *Ann Thorac Surg* 2019;108:1459–1466. doi:10.1016/j.athoracsur.2019.04.116.
6. Valdis M, Chu MW, Schlachta C, et al. Evaluation of robotic cardiac surgery simulation training: A randomized controlled trial. *J Thorac Cardiovasc Surg* 2016;151:1498–1505. doi:10.1016/j.jtcvs.2016.02.016.
7. Trehan K, Kemp CD, Yang SC. Simulation in cardiothoracic surgical training: where do we stand? *J Thorac Cardiovasc Surg* 2014;147:18–24. doi:10.1016/j.jtcvs.2013.09.007.
8. Jung C, Wolff G, Wernly B, et al. Virtual and Augmented Reality in Cardiovascular Care: State-of-the-Art and Future Perspectives. *JACC Cardiovasc Imaging* 2022;15:519–532. doi:10.1016/j.jcmg.2021.08.017.
9. Pelargos PE, Nagasawa DT, Lagman C, et al. Utilizing virtual and augmented reality for educational and clinical enhancements in neurosurgery. *J Clin Neurosci* 2017;35:1–4. doi:10.1016/j.jocn.2016.09.002.
10. Niederer SA, Lumens J, Trayanova NA. Computational models in cardiology. *Nat Rev Cardiol* 2019;16:100–111. doi:10.1038/s41569-018-0104-y.
11. Paulus CJ, Haouchine N, Kong SH, et al. Handling topological changes during elastic registration. *Int J Comput Assist Radiol Surg* 2017;12:461–470. doi:10.1007/s11548-016-1493-1.
12. Faure F, Duriez C, Delingette H, et al. SOFA: A multi-model framework for interactive physical simulation. *Soft Tissue Biomech Model Comput Assist Surg* 2012;11:283–321. doi:10.1007/8415\_2012\_125.
13. Zeng H, Zhang X, Chen J, et al. A Liver Electrosurgery Simulator Developed by Unity Engine. In: Proceedings of International Conference on Biomedical Signal and Image Processing 2021:14–19. doi:10.1145/3477187.3477193.
14. Qian K, Wang M, Cui Y. Simulation ready anatomy model generation pipeline for virtual surgery. *Comput Animat Virtual Worlds* 2021. doi:10.1002/cav.2016.

- 560 15. Moore J, Scheirich H, Jadhav S, et al. The interactive medical simulation toolkit (iMSTK): An open source platform for surgical  
561 simulation. *Front Virtual Real* 2023;4:1130156. doi:10.3389/frvir.2023.1130156.
- 562 16. Okamura AM. Haptic feedback in robot-assisted minimally invasive surgery. *Curr Opin Urol* 2009;19:102-107.  
563 doi:10.1097/MOU.0b013e32831a478c.
- 564 17. Pacchierotti C, Prattichizzo D, Kuchenbecker KJ. Cutaneous feedback of fingertip deformation and vibration for palpation in  
565 robotic surgery. *IEEE Trans Biomed Eng* 2016;63:278-287. doi:10.1109/TBME.2015.2455932.
- 566 18. Cardoso MJ, et al. Monai: An open-source framework for deep learning in healthcare. *arXiv preprint arXiv:2211.02701* 2022.
- 567 19. Kong F, Shadden SC. Learning Whole Heart Mesh Generation From Patient Images for Computational Simulations. *IEEE Trans  
568 Med Imaging* 2023;42:533-545. doi:10.1109/TMI.2022.3219284.
- 569 20. Updegrafe A, et al. SimVascular: an open source pipeline for cardiovascular simulation. *Ann Biomed Eng* 2017;45:525-541.  
570 doi:10.1007/s10439-016-1762-8.

571

572 **Disclaimer/Publisher's Note:** The statements, opinions and data contained in all publications are solely those of the  
573 individual author(s) and contributor(s) and not of MDPI and/or the editor(s). MDPI and/or the editor(s) disclaim re-  
574 sponsibility for any injury to people or property resulting from any ideas, methods, instructions or products referred to  
575 in the content.